Journal of Hazardous Materials 488 (2025) 137314

Contents lists available at ScienceDirect

Journal of Hazardous Materials

journal homepage: www.elsevier.com/locate/jhazmat

Mapping nutrient pollution in inland water bodies using multi-platform hyperspectral imagery and deep regression network

Chao Niu [a,b], Kun Tan [a,b,*], Xue Wang [a,b], Chen Pan [c]

[a] Key Laboratory of Geographic Information Science (Ministry of Education), East China Normal University, Shanghai 200241, China
[b] Key Laboratory of Spatial-Temporal Big Data Analysis and Application of Natural Resources in Megacities (Ministry of Natural Resources), East China Normal University, Shanghai 200241, China
[c] Shanghai Municipal Institute of Surveying and Mapping, Shanghai, 200063, China

HIGHLIGHTS

- A novel deep learning framework for water quality monitoring is proposed.
- Deep regression outperforms traditional methods in water quality estimation.
- Achieved accurate concentration mapping using airborne hyperspectral imagery.
- The model applies to satellite hyperspectral imagery for long-term monitoring.

GRAPHICAL ABSTRACT

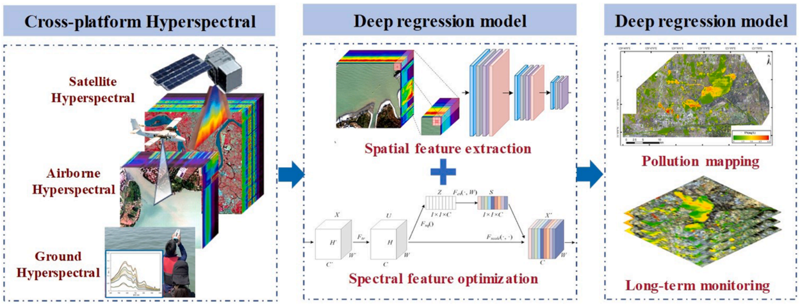

ARTICLE INFO

Keywords:
Inland water quality
Hyperspectral remote sensing
Deep regression network
Spatial-spectral joint learning

ABSTRACT

Inland waters face multiple threats from human activities and natural factors, leading to frequent water quality issues, particularly the significant challenge of eutrophication. Hyperspectral remote sensing provides rich spectral information, enabling timely and accurate assessment of water quality status and trends. To address the challenge of inaccurate water quality mapping, we propose a novel deep learning framework for multi-parameter estimation from hyperspectral imagery. A deep convolutional spatial-spectral joint learning method incorporating high-dimensional attention-weighted differences is proposed to optimize the deep features. The model was used to accurately estimate the distribution of three key eutrophication-related water quality parameters: total nitrogen, total phosphorus, and ammonia nitrogen. Through scale analysis, ablation experiments, and model comparisons, the results demonstrate stable regression performance with the proposed model. Specifically, the coefficient of determination (R2) values are 0.8315, 0.8137, and 0.8245, the mean absolute error (MAE) values are 0.2035, 0.0056 and 0.0134, and the mean squared error (MSE) values are 0.0733, 0.00008 and 0.0003 for the three parameters in the test set, respectively. Compared to the traditional feature analysis and regression methods, the R^2 values are improved by approximately 30 %, while the MAE and MSE values are reduced by approximately 60 % and 80 %, respectively. The model was applied to airborne hyperspectral imagery for nutrient pollution mapping. To assess the model's generalizability, we applied the trained model to multi-

---

* Corresponding author at: Key Laboratory of Geographic Information Science (Ministry of Education), East China Normal University, Shanghai 200241, China.
E-mail address: tankuncu@gmail.com (K. Tan).

https://doi.org/10.1016/j.jhazmat.2025.137314
Received 25 November 2024; Received in revised form 9 January 2025; Accepted 20 January 2025

temporal satellite hyperspectral imagery and validated against in situ monitoring data, where the proposed model demonstrated promising cross-platform and temporal transferability.

1. Introduction

Inland water bodies playing a vital role in regulating the global biogeochemical cycles, regional climate, and ecosystem balance [1]. However, these vital ecosystems are vulnerable to both human activities and natural disturbances, leading to frequent occurrences of organic and inorganic pollution, eutrophication, and harmful algal blooms. In particular, many rivers and lakes are now suffering from eutrophication, a condition often characterized by excessive water quality parameters such as total nitrogen (TN), total phosphorus (TP), and ammonia nitrogen (NH3-N) [2,3]. This poses a critical challenge to maintaining water quality and ecosystem health. Therefore, the ability to conduct dynamic monitoring and achieve accurate estimation of water quality parameters is crucial for assessing regional water health and guiding effective river basin management, providing a basis for subsequent analysis and management [4].

Remote sensing technology has been extensively applied in inland water monitoring. The primary objective is to utilize the water radiative signals received by sensors to explore the relationship with water quality parameters, thereby enabling the construction of remote sensing based estimation models. These nutrients are crucial indicators for assessing water eutrophication and pose significant challenges for remote sensing monitoring. Differing from water color parameters such as chlorophyll-a (Chl-a), colored dissolved organic matter (CDOM), and total suspended matter (TSM), these parameters are optically inactive, making it challenging to directly establish a connection between these parameters and remote sensing reflectance [5]. Most studies have indirectly estimated these parameters by analyzing their intrinsic correlation with water color parameters [6-8]. Recent advancements in machine learning have shown promise in improving the accuracy of estimating optically inactive parameters using multispectral imagery [9,10]. However, it remains challenging to model the complex nonlinear relationships between apparent optical properties and water quality parameters. Traditional regression techniques often fail to capture these complexities, posing significant challenges for accurate water quality estimation.

Hyperspectral data obtain the spatial information of ground objects as well as multiple continuous spectral bands. They can capture the fine spectral characteristics of water bodies, and differentiated spectral characteristics provide possibilities for quantitatively characterizing the different water quality states [11]. Statistical learning-based feature analysis, including feature selection and feature extraction, is a common approach in hyperspectral regression. Feature selection aims to identify relevant subsets of spectral features [12], while feature extraction transforms the original features into a more informative set [13]. Machine learning regression models have demonstrated distinct advantages in solving complex nonlinear problems with a limited sample size. Partial least squares regression (PLSR), support vector regression (SVR), random forest (RF), and other machine learning methods have been widely used in water quality monitoring [14,15]. However, these they often struggle to fully utilize hyperspectral data’s spectral and spatial correlations, limiting their accuracy. The deep learning based regression models characterize the mapping relationship between the spectra and water quality parameters through multi-layer nonlinear transformations. Some patch-based deep networks can simultaneously consider the spatial and spectral information of images, exhibiting superior expressive ability in hyperspectral interpretation tasks [16]. In addition, the attention mechanism in deep learning can dynamically assign weights in the spatial and channel dimensions, reducing the computational overhead and improving the model performance [17]. Balancing model complexity and generalization when training with limited annotated data is a major challenge in regression modeling for water quality estimation.

Currently, the primary data source for hyperspectral water quality estimation is airborne platforms, which have been widely applied in small- and medium-scale water environment monitoring. With the attribute of superior spatial-spectral resolution, airborne hyperspectral imagery is capable of more precisely identifying the radiative information of water bodies, leading to accurate quantification of multiple parameters [18-20]. Recently, a series of hyperspectral satellites have been successfully launched, such as GF-5, EnMap, PRISMA, ZY1–02D, and ZY1–02E. These new hyperspectral satellites have greatly enriched the diversity and accessibility of hyperspectral data, enabling expanded applications in water environment monitoring. Compared to airborne hyperspectral platforms, satellite hyperspectral platforms have a larger swath width and fixed revisit cycle, along with a lower acquisition cost, which confers advantages for long-term monitoring of inland waters. Considering the distinct characteristics of airborne and spaceborne data, the integration of cross-platform hyperspectral data for water quality monitoring has become a major focus. However, sensor performance and external imaging environments limit the cross-platform transferability of the data-driven modeling methods. How to construct the complex mapping relationship between spectra and water quality parameters, while maintaining the stability and applicability of the algorithms, is another challenge limiting the application of hyperspectral water environment monitoring.

Based on this, a deep convolutional spatial-spectral joint learning method based on high-dimensional attention difference weights was constructed in this study to learn the spatial characteristic correlation and channel feature dependence of hyperspectral image data. This approach can achieve spatial-spectral sensitive feature optimization based on hyperspectral imagery, thus improving the reliability and robustness of the model. The proposed method was utilized to estimate TN, TP, and NH3-N, enabling accurate mapping of nutrient pollution and a detailed analysis of water quality in the study area. This is crucial for understanding the spatial distribution and sources of these pollutants within aquatic ecosystems, ultimately supporting effective water resource management and environmental protection. To further evaluate the method’s robustness, a multi-platform and multi-temporal applicability analysis was performed to assess the model’s transferability. The improved capability to map nutrient pollution provide valuable information for pinpointing areas requiring urgent attention and intervention. This detailed spatial information can directly contribute to improving water management strategies by enabling targeted interventions. Furthermore, by visualizing the extent and severity of nutrient pollution, this research can support policymakers in developing and implementing effective strategies for eutrophication mitigation, ultimately leading to better informed decisions concerning water quality and ecosystem health.

2. Materials

2.1. Research area

The research area is located within the Yangtze River Delta Integrated Development Demonstration Zone, situated at the intersection of the city of Shanghai, Jiangsu and Zhejiang provinces in China. The acquired hyperspectral image data cover an area of approximately 800 km^2, encompassing the key cross-provincial water bodies, including the Taipu River, Dianshan Lake, Yuandang Lake, and Fenhu Lake, which are collectively known as “One River and Three Lakes”.

Dianshan Lake and Yuandang Lake are situated within the Taihu Basin, which is a natural freshwater lake region in the river plain area.

Table 1
AMMIS spectrometer parameters.

Parameter	VNIR	SWIR
Spectral range / nm	400–1000	950–2500
Number of bands	256	256
Spectral resolution / nm	< 5 nm	< 5 nm
FOV / °	40	40
IFOV / mrad	≤ 0.25	≤ 0.5
Signal-to-noise ratio	≧ 500	≧ 300

Table 2
AHSI spectrometer parameters.

Parameter	ZY1-02D, 02E
Orbital altitude / km	778
Revisit period / days	55
Spatial resolution / m	30
Swath width / km	60
Spectral range / nm	400–2500
Spectral resolution / nm	10 VNIR / 20 SWIR
Number of bands	166
Signal-to-noise ratio	≥ 240 (0.4–0.9 μm) ≥ 180 (0.9–1.75 μm) ≥ 120 (1.75–2.50 μm)

Table 3
Satellite image acquisition information.

Parameter	Acquisition date				
	2021/11/18	2022/12/25	2022/12/25	2023/03/06	2023/03/06
Satellite	ZY1–02D	ZY1–02D	ZY1–02 D	ZY1–02E	ZY1–02E
Acquisition time (UTC+8)	10:48:16	10:56:01	10:56:08	10:58:13	10:58:21
Center coordinates	31.17°N, 121.11°E	31.29°N, 120.92°E	30.85°N, 120.80°E	31.61°N, 121.14°E	30.83°N, 121.02°E

These lakes are hydrologically connected to the Taihu water system. Wastewater discharge from industrial and aquaculture activities has led to water quality degradation [21]. Furthermore, the surface sediment of Dianshan Lake has a relatively high TN content, while Yuandang Lake exhibits severe organic matter pollution in the bottom sediments, resulting in high nitrogen and phosphorus loading and severe eutrophication in these lake systems [22].

2.2. *Hyperspectral image acquisition*

The airborne hyperspectral images were acquired using a fixed-wing aircraft equipped with the Airborne Multi-Modality Imaging Spectrometer (AMMIS). Imaging spectrometer parameters are provided in Table 1. Hyperspectral data were collected over the period from June 15 to June 16, 2022, achieving an image spatial resolution of 0.75 m. Given the weak reflectance signals from water bodies beyond 1000 nm, the visible and near-infrared (VNIR) bands were utilized for the subsequent experiments.

Satellite hyperspectral imagery data acquired from the Advanced Hyperspectral Imager (AHSI) sensors mounted on the ZY1–02D and ZY1–02E were used for the model validation and long-term application experiments. The ZY1–02D and ZY1–02E were launched on September 12, 2019, and December 26, 2021, respectively, achieving a dual-satellite network for joint observation, which enhances the revisit capabilities and observation frequency. The AHSI spectrometer parameters are listed in Table 2. By selecting images that covered the study area and were free of cloud and fog cover, a total of five images from three periods were obtained for the inversion applications. The specific imaging times and corresponding satellite information are provided in Table 3.

2.3. *Sample acquisition and laboratory testing*

Water samples and in situ spectra were collected quasi-synchronously with airborne imagery, resulting in a total of 61 sets. The columnar water samples were acquired at a depth below 50 cm. The above-water approach was used for measuring the water spectra. The sampling distribution is illustrated in Fig. 1, which were mainly distributed around the Dianshan and Yuandang Lake area, and along the Taipu River within Shanghai.

The concentrations of TN, TP, and NH3-N were measured using a HACH DR3900 spectrophotometer. The measurement of TN and TP involved a digestion process using a digestion instrument, with TN and TP measured using the persulfate digestion method and ascorbic acid method, respectively. NH3-N was determined using the salicylic acid method. In addition, to ensure the reliability of the measurement results, parallel samples were set up for quality control during the testing, and the results of the standard sample testing were compared to verify the

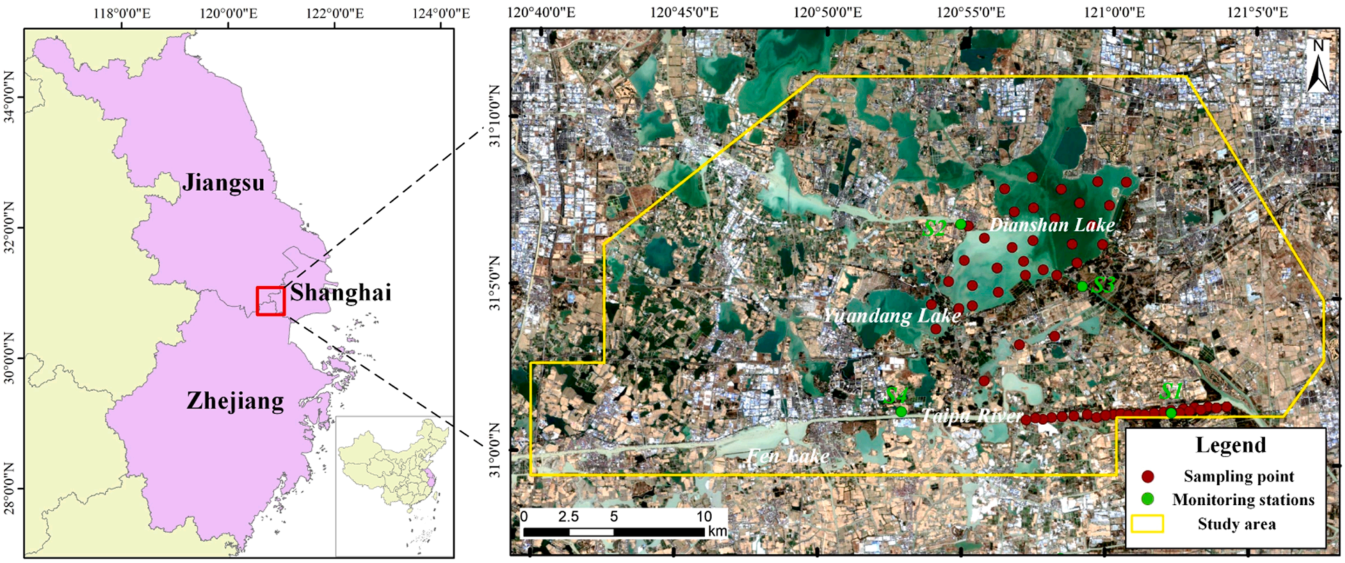

Fig. 1. Location of the research area.

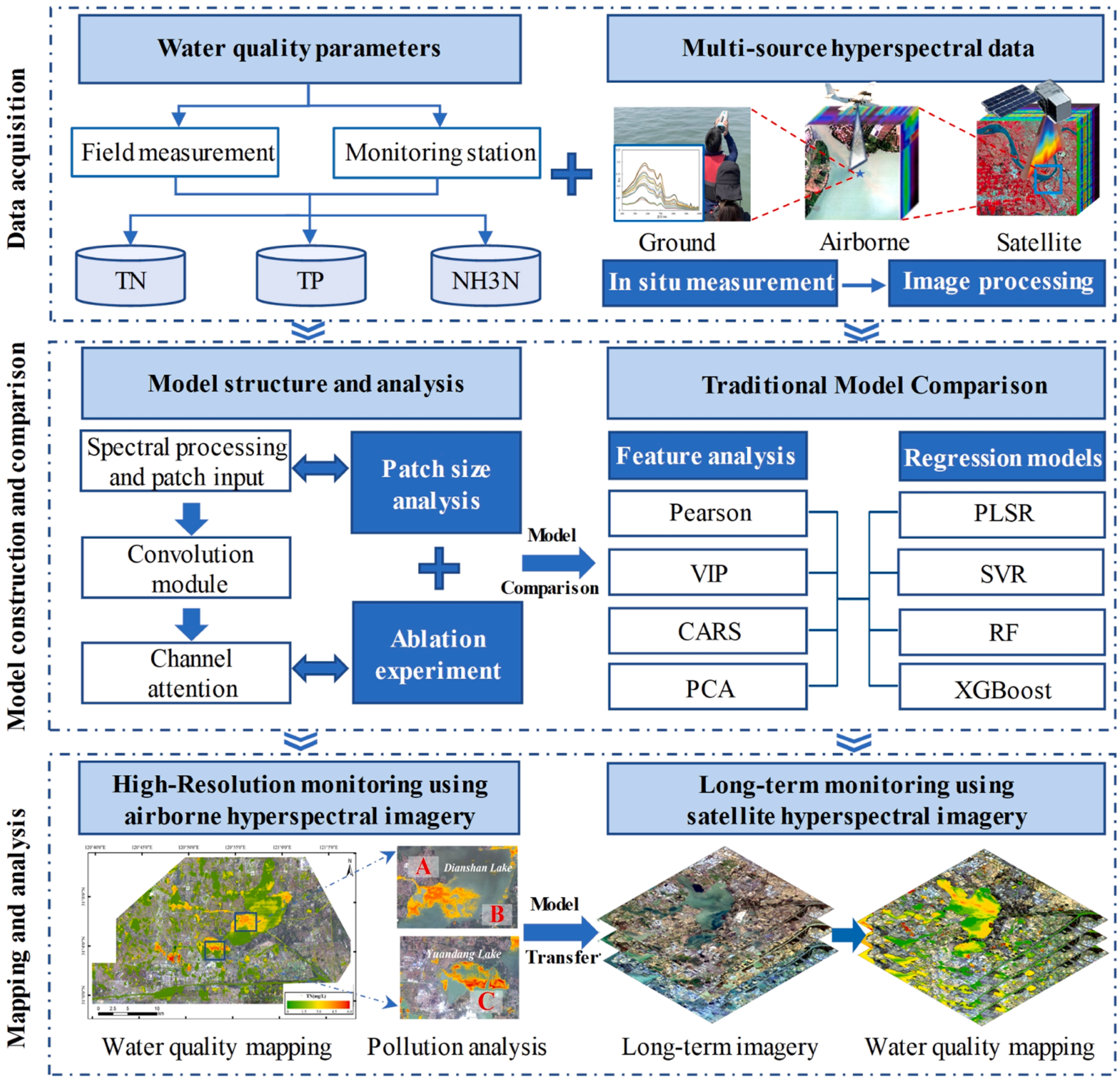

Fig. 2. Schematic flow of the study.

measurements.

3. Method

In this study, to achieve accurate estimation of multiple water quality parameters, we utilized field measured and monitoring station water quality data, in conjunction with multi-source hyperspectral remote sensing data derived from “ground-aerial-satellite” observations. The schematic flow of the study is shown in Fig. 2.

3.1. Image processing

The MODTRAN radiative transfer model was used to perform atmospheric correction on both airborne and satellite images. The top-of-atmosphere radiance data were obtained after vicarious calibration of both the airborne and satellite hyperspectral imagery [23]. In addition, bidirectional reflectance distribution function (BRDF) correction was also applied to eliminate the BRDF effect for the airborne hyperspectral imagery [24].

3.2. Spectral pre-processing

The remote sensing reflectance inevitably contains some noise interference, which can be mitigated through spectral pre-processing to reduce errors resulting from incomplete image correction. We performed first-order differential processing on the spectra, which can eliminate background signal interference and highlight the spectral characteristics.

3.3. Patch-based channel attention deep neural network regression (Patch-CA-DNNR)

Considering the high-dimensional spatial-spectral characteristics of hyperspectral imagery, Patch-CA-DNNR utilizes image patch inputs and convolution operations to learn the local spatial connections of the high-dimensional spectral channels, enabling the extraction of fused features of the spatial texture and spectral channels. To enhance the feature extraction capability of the network for the spectral channel and improve the robustness and interpretability of the model, a squeeze-and-excitation (SE) module [25] is used to adaptively adjust the channel weights. By modeling the degree of correlation between the features after convolution processing, the SE module adaptively adjusts the channel weights, allowing for a depiction of the significance of the feature information.

Considering the uncertainty of deep networks in small sample regression tasks, and to avoid overfitting caused by excessive network layer numbers and training difficulties caused by mismatched model complexity and data volume, a lightweight network structure with

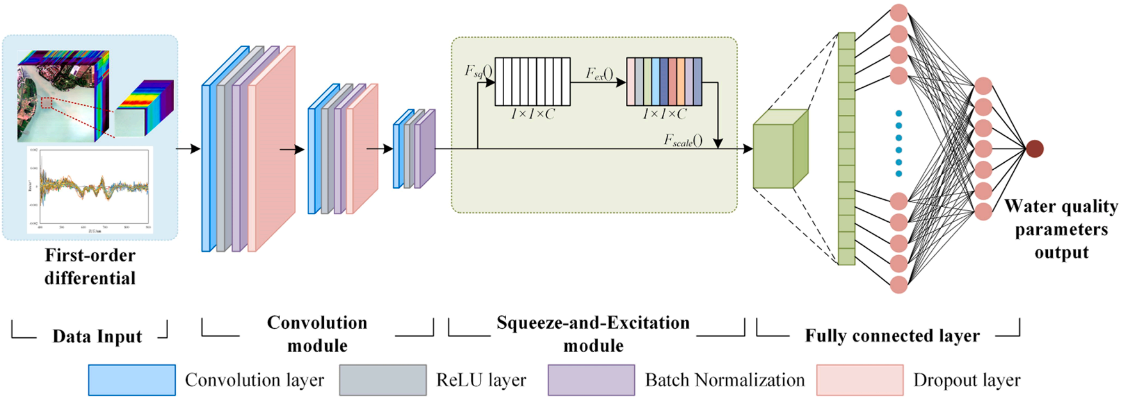

Fig. 3. Patch-CA-DNNR structure for estimating water quality parameters.

relatively few network layers was designed. This network structure can better balance the model's expressive ability and generalization ability with limited sample quantities. The overall network architecture includes three convolutional layers, with a step size of 1 in the convolution calculation. The first convolution kernel size is 3 × 3, and the rest are 2 × 2. After the convolution operation, a rectified linear unit (ReLU) is used as the activation function, while batch normalization is conducted simultaneously. In addition, to improve the model's generalization ability and prevent overfitting, random dropout layers are introduced before the second and third convolution operations. The structure of Patch-CA-DNNR is illustrated in Fig. 3.

During the training process, the learning rate was initially set to 0.01, and a step learning rate (StepLR) schedule was applied to dynamically adjust the learning rate. The maximum iterations were set to 500.

3.4. *Methodological comparison*

3.4.1. *Deep learning based regression model*

We assessed the contribution of the channel attention module in the deep regression network by conducting ablation experiments. The ablation experiments used the same framework as Patch-CA-DNNR, but with the SE module removed, which we named the Patch-DNNR model.

Furthermore, to compare the model performance when considering spatial features in the patch inputs versus not considering spatial features in the pixel inputs in the water quality parameter estimation task, we designed a pixel-based deep regression network (Pixel-DNNR). The network layers were consistent with Patch-CA-DNNR, but the convolutional layers were replaced with fully connected layers.

3.4.2. *Traditional feature analysis and machine learning regression methods*

In order to further verify the ability of deep feature mining to estimate water quality parameters, a total of 16 model combinations, using the four traditional feature analysis methods with four machine learning regression modeling methods, were applied to estimate the three parameters.

3.4.2.1. *Feature analysis methods.*

(1) Pearson correlation coefficient

The Pearson correlation coefficient statistically characterizes the strength and direction of the linear association between variables using the covariance and standard deviation. The correlation coefficient r is calculated as follows:

$$r=\frac{\text{cov}(x,y)}{\sigma_x\sigma_y}=\frac{\sum_{i=1}^{n}(x_i-\overline{x})(y_i-\overline{y})}{\sqrt{\sum_{i=1}^{n}(x_i-\overline{x})^2}\sqrt{\sum_{i=1}^{n}(y_i-\overline{y})^2}}, \tag{1}$$

where n is the sample size, x_i and y_i are the variable values of sample i, and $\overline{x}$ and $\bar{y}$ are the sample means. In this experiment, the r value was used for the feature band selection, while a minimum wavelength interval was set to avoid redundancy of the adjacent wavelength features.

(2) Variable influence on projection (VIP)

VIP is a parameter used to calculate the cumulative influence of the independent variable x on the model, and represents the importance of a variable in explaining the dependent variable [26]. The importance VIP_i of feature band i is as calculated follows:

$$VIP_i=\sqrt{\frac{p\sum_{h=1}^{n}r^2(y,c_h)w^2{}_{hj}}{\sum_{h=1}^{n}r^2(y,c_h)}} \tag{2}$$

where p is the number of predictor variables, y is the dependent variable, n is the number of principal components, w_{hj} is the weight of the independent variable for the h-th principal component, and r^2 represents the square of the correlation coefficient. A larger VIP value indicates higher importance.

After completing the importance calculation for the feature bands, feature selection was performed using a similar method to the Pearson correlation analysis, with the following steps:

(a) All feature bands with VIP values greater than 0.7 were selected as the candidate subset.
(b) The wavelengths of the candidate subset were examined, using a minimum interval of 5 nm to further select the band with the maximum correlation coefficient.
(c) The feature combinations were sorted in order of VIP values to form a new feature subset.

(3) Competitive adaptive reweighted sampling (CARS)

The CARS treats each variable as an independent individual. It utilizes PLSR to assess the regression coefficients, and sequentially removes variables with smaller absolute values, thereby eliminating the "unfit" individuals. The selected feature set was obtained following the steps outlined in Tan et al. [27].

Table 4
Estimation accuracy of the three water quality parameters using different input patch scales.

Water quality parameter	Patch size	Training set			Test set		
		R^2	MAE	MSE	R^2	MAE	MSE
TN	**5 × 5**	**0.8777**	**0.3562**	**0.2342**	**0.8315**	**0.2035**	**0.0733**
	9 × 9	0.8431	0.3793	0.3079	0.8169	0.2174	0.0805
	13 × 13	0.8172	0.4222	0.3588	0.7971	0.2398	0.0892
	17 × 17	0.8833	0.3389	0.2291	0.7646	0.2493	0.1035
	21 × 21	0.8769	0.3424	0.2416	0.7582	0.2620	0.1063
TP	**5 × 5**	**0.8677**	**0.0058**	**0.00006**	**0.8137**	**0.0056**	**0.00006**
	9 × 9	0.8150	0.0074	0.00008	0.7661	0.0067	0.00007
	13 × 13	0.7396	0.0083	0.00009	0.7322	0.0076	0.00007
	17 × 17	0.7312	0.0073	0.00012	0.6985	0.0081	0.00009
	21 × 21	0.7615	0.0081	0.00010	0.7524	0.0070	0.00007
NH3-N	**5 × 5**	**0.8955**	**0.0136**	**0.0004**	**0.8245**	**0.0134**	**0.0003**
	9 × 9	0.6902	0.0235	0.0009	0.6524	0.0214	0.0009
	13 × 13	0.6128	0.0274	0.0014	0.6115	0.0173	0.0005
	17 × 17	0.5147	0.0264	0.0013	0.5117	0.0265	0.0015
	21 × 21	0.6384	0.0240	0.0012	0.6317	0.0175	0.0006

Table 5
Estimation accuracy using the different deep regression models.

Water quality parameter	Deep regression model	Training set			Test set		
		R^2	MAE	MSE	R^2	MAE	MSE
TN	**Patch-CA-DNNR**	**0.8777**	**0.3562**	**0.2342**	**0.8315**	**0.2035**	**0.0733**
	Patch-DNNR	0.7876	0.4821	0.4169	0.7593	0.2544	0.1058
	Pixel-DNNR	0.5743	0.6821	0.8354	0.5381	0.3421	0.2031
TP	**Patch-CA-DNNR**	**0.8677**	**0.0058**	**0.00006**	**0.8137**	**0.0056**	**0.00008**
	Patch-DNNR	0.8124	0.0064	0.00008	0.7361	0.0075	0.00008
	Pixel-DNNR	0.6144	0.0097	0.00017	0.6384	0.0084	0.00010
NH3-N	**Patch-CA-DNNR**	**0.8955**	**0.0136**	**0.0004**	**0.8245**	**0.0134**	**0.0003**
	Patch-DNNR	0.6456	0.0240	0.0012	0.6317	0.0175	0.0006
	Pixel-DNNR	0.7414	0.0230	0.0008	0.7058	0.0158	0.0004

(4) Principal component analysis (PCA)

PCA has been widely applied in hyperspectral feature extraction because of its excellent dimensional reduction and denoising capabilities. By setting the principal component variance and the minimum proportion threshold, the number of principal components can be determined.

3.4.2.2. Machine learning regression methods. After the feature analysis, four machine learning regression methods—PLSR, SVR, RF, and extreme gradient boosting (XGBoost)—were used for the comparative analysis. These models were chosen to represent a diverse set of machine learning approaches, including a linear method (PLSR), a kernel-based method (SVR), and two ensemble methods (RF and XGBoost). The codes are available directly in the open-source scikit-learn and xgboost Python libraries. Five-fold cross-validation was conducted during the model training, and the hyperparameters of each regressor were optimized using grid search. In the RF and XGBoost models, the random state was set to a fixed value of 42.

(1) PLSR

PLSR is a statistical method that explores the interrelationships among multiple correlated variables. It leverags PCA to transform original variables into principal components for regression analysis, thereby mitigating multicollinearity [28]. In hyperspectral image regression tasks, given an input spectral matrix X and the corresponding water quality parameter Y, PLSR operates by performing PCA on both X and Y and subsequently determining the correlation matrix between their respective latent variables.

(2) SVR

SVR extends the Support Vector Machine (SVM) algorithm to regression problems. It aims to find an optimal hyperplane in a high-dimensional feature space that minimizes the prediction error while simultaneously maximizing the margin, which is the distance between the hyperplane and the closest data points [29].

Given a sample space $[(x_1, y_1),\ldots,(x_n, y_n)]$, where x_i represents the features and y_i denotes the observed data, SVR employs an ε-insensitive loss function for error measurement. In the context of non-linear conditions, the model introduces slack variables and a penalty coefficient to optimize the non-linear problem. This is achieved by seeking the optimal support vector w such that the function $f(x)=wx+b$ minimizes the regression error while maximizing the margin.

(3) RF

RF is an ensemble learning method that utilizes decision trees as base learners. The final prediction is obtained by averaging the predictions of these trees, representing a typical Bagging approach in ensemble learning [30]. In the construction of each tree, a random subset of features is considered at each node split. This random feature selection reduces the correlation between trees, leading to lower variance in the ensemble's predictions compared to a single decision tree.

(4) XGBoost

XGBoost is also an ensemble learning method that utilizes decision trees as base learners. Different from the Bagging strategy used by RF, XGBoost adopts a Boosting approach, sequentially organizing weak regression decision trees to form a strong regression model [31]. The Boosting algorithm initially trains a decision tree on the complete dataset. Subsequent learners then adjust the dataset weights based on the "bias" predicted by the preceding model for their training. Each tree is assigned a weight in the final ensemble based on its performance. The final prediction is a weighted sum of the predictions from all the trees.

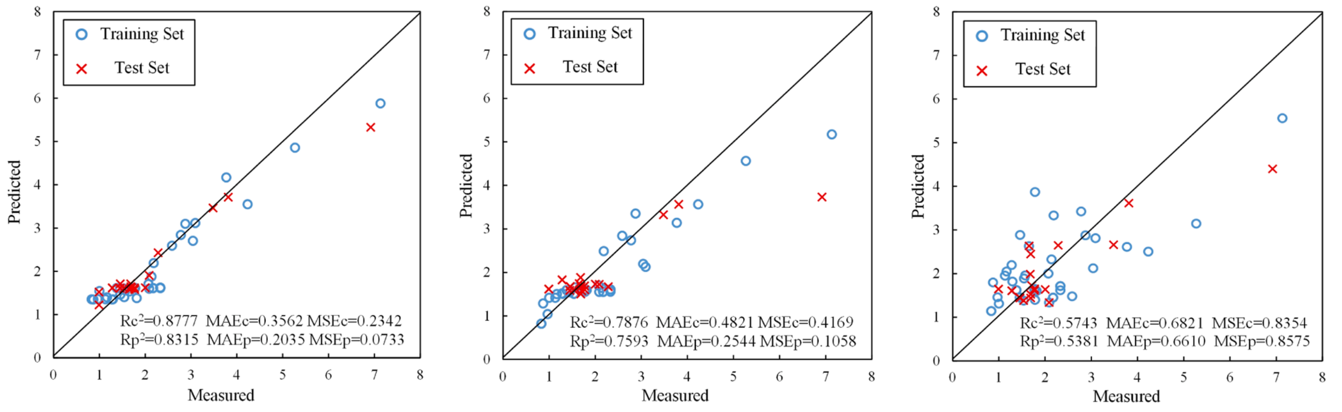

(a) TN: Patch-CA-DNNR (b) TN: Patch-DNNR (c) TN: Pixel-DNNR

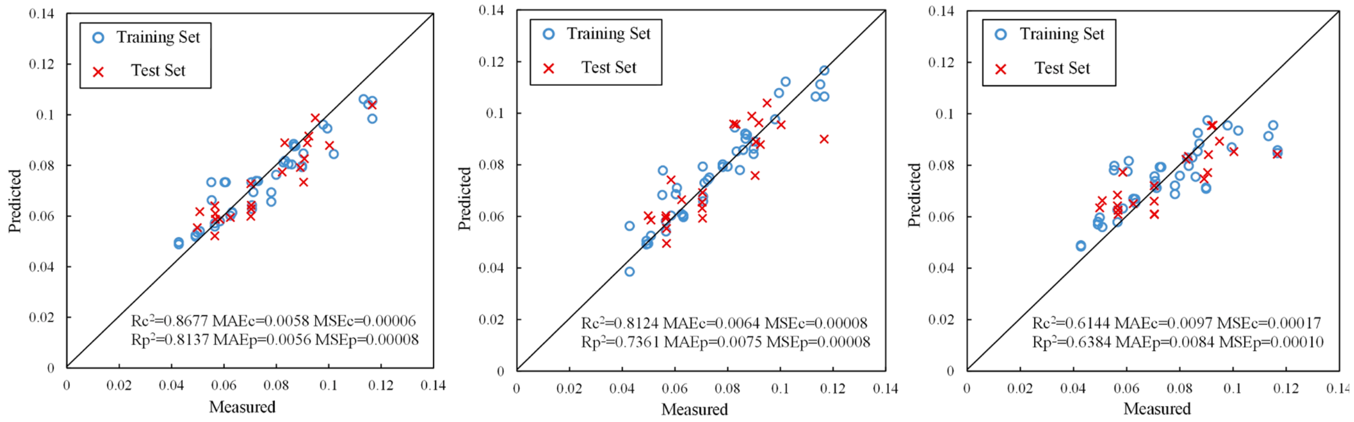

(d) TP: Patch-CA-DNNR (e) TP: Patch-DNNR (f) TP: Pixel-DNNR

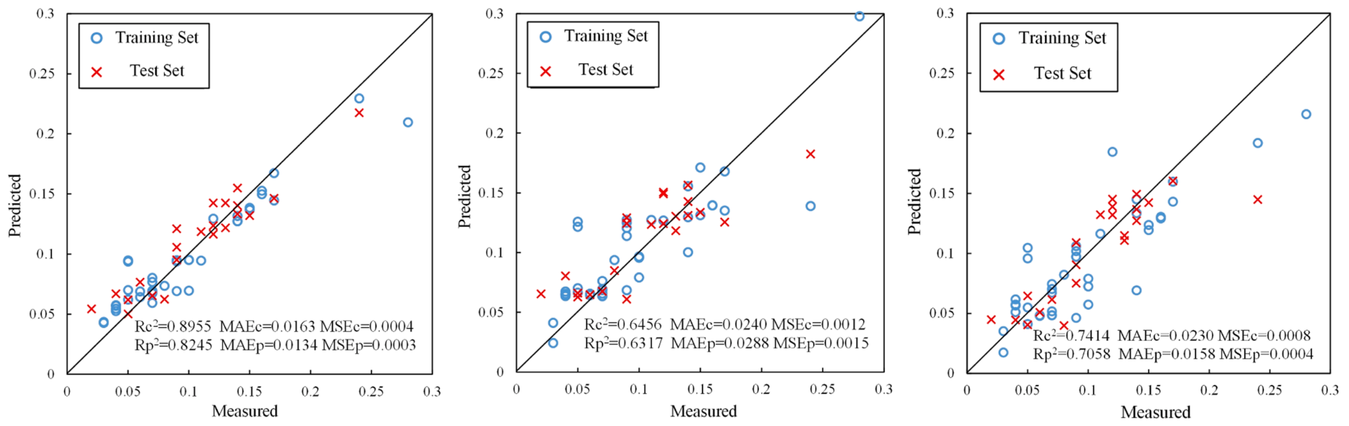

(g) NH3-N: Patch-CA-DNNR (h) NH3-N: Patch-DNNR (i) NH3-N: Pixel-DNNR

Fig. 4. Scatter plots of the estimated results obtained by the deep regression models.

3.5. Model evaluation

The dataset was split randomly into training and testing subsets at a 2:1 ratio, with the evaluation indices including the coefficient of determination (R^2), mean squared error (MSE), and mean absolute error (MAE).

$$R^2 = 1 - \frac{\sum_{i=1}^{n} (\widehat{y}_i - y_i)^2}{\sum_{i=1}^{n} (\overline{y}_i - y_i)^2} \tag{3}$$

$$MSE = \frac{1}{n} \sum_{i=1}^{n} (\widehat{y}_i - y_i)^2 \tag{4}$$

Table 6
Comparison of the estimation accuracy using the different feature analysis methods.

Water quality parameter	Feature analysis method	Regression model	Training set			Test set		
			R^2	MAE	MSE	R^2	MAE	MSE
TN	Pearson	PLS	0.3457	0.6261	0.8117	0.2264	0.8757	1.4444
		SVR	0.2739	0.5722	0.9007	0.2625	0.8018	1.3771
		RF	0.3636	0.5902	0.7895	0.3279	0.7801	1.2549
		XGB	0.7318	0.3805	0.3327	0.0398	0.8447	1.7928
	VIP	PLS	0.7810	0.4019	0.2717	0.1095	1.3855	3.4072
		SVR	0.2214	0.5837	0.9659	0.2368	0.8152	1.4249
		RF	0.3702	0.5876	0.7814	0.2547	0.8394	1.3915
		XGB	0.4903	0.5527	0.6323	0.0331	0.9268	1.8053
	CARS	PLS	0.1990	0.6304	0.9937	0.1348	0.8956	1.6154
		SVR	0.1828	0.5842	1.0138	0.0452	0.8287	1.7827
		RF	0.5645	0.4756	0.5403	0.2372	0.8442	1.4242
		XGB	0.5252	0.5167	0.5890	0.2879	0.8216	1.3295
	PCA	PLS	0.4053	0.5998	0.7377	0.1323	0.8743	1.6201
		SVR	0.2645	0.5756	0.9125	0.1285	0.8239	1.6273
		RF	0.8372	0.3396	0.2019	0.5097	0.6936	0.9154
		XGB	**0.9684**	**0.1518**	**0.0392**	**0.5497**	**0.6473**	**0.8408**
TP	**Pearson**	PLS	0.2298	0.0126	0.0002	0.1758	0.0151	0.0004
		SVR	0.0437	0.0151	0.0003	0.0499	0.0206	0.0005
		RF	0.6467	0.0080	0.0001	0.3428	0.0135	0.0003
		XGB	**0.9926**	**0.0012**	**0.0001**	**0.4348**	**0.0130**	**0.0003**
	VIP	PLS	0.7894	0.0066	0.0001	0.1292	0.0157	0.0005
		SVR	0.0499	0.0151	0.0003	0.0437	0.0206	0.0005
		RF	0.4689	0.0104	0.0002	0.3746	0.0126	0.0003
		XGB	0.9355	0.0031	0.0001	0.3454	0.0143	0.0003
	CARS	PLS	0.5310	0.0098	0.0001	0.3778	0.0126	0.0003
		SVR	0.0499	0.0151	0.0003	0.0437	0.0206	0.0005
		RF	0.8106	0.0058	0.0001	0.2110	0.0151	0.0004
		XGB	0.9810	0.0016	0.0001	0.0291	0.0162	0.0005
	PCA	PLS	0.4139	0.0110	0.0002	0.3034	0.0139	0.0004
		SVR	0.0499	0.0151	0.0003	0.0537	0.0206	0.0005
		RF	0.8006	0.0056	0.0001	0.3701	0.0136	0.0003
		PLS	0.2298	0.0126	0.0002	0.1758	0.0151	0.0004
NH3-N	**Pearson**	PLS	0.3531	0.0304	0.0017	0.3717	0.0342	0.0019
		SVR	0.3271	0.0324	0.0018	0.3769	0.0361	0.0018
		RF	**0.8088**	**0.0171**	**0.0005**	**0.4488**	**0.0327**	**0.0016**
		XGB	0.9110	0.0125	0.0002	0.3908	0.0330	0.0018
	VIP	PLS	0.7790	0.0193	0.0006	0.0153	0.1001	0.0153
		SVR	0.0534	0.0526	0.0041	0.0492	0.0555	0.0044
		RF	0.3401	0.0294	0.0018	0.0707	0.0404	0.0028
		XGB	0.0870	0.0402	0.0027	0.0751	0.0456	0.0030
	CARS	PLS	0.4037	0.0303	0.0016	0.4259	0.0305	0.0017
		SVR	0.0309	0.0467	0.0032	0.0232	0.0503	0.0039
		RF	0.6552	0.0236	0.0009	0.2779	0.0348	0.0021
		XGB	0.9685	0.0066	0.0001	0.2896	0.0359	0.0021
	PCA	PLS	0.3579	0.0310	0.0017	0.3214	0.0343	0.0020
		SVR	0.3489	0.0306	0.0017	0.3759	0.0338	0.0018
		RF	0.7621	0.0165	0.0006	0.3875	0.0318	0.0018
		XGB	0.9665	0.0055	0.0001	0.3319	0.0329	0.0020

$$MAE = \frac{1}{n}\sum_{i=1}^{n}|\widehat{y}_i - y_i| \tag{5}$$

where y_i refers to the measured value, $\widehat{y}_i$ is the predicated value. n is the total number of sample points.

The R^2 value closer to 1 indicates a higher degree of model fit accuracy. In the field of water quality monitoring, the R^2 value greater than 0.6 indicates that the model possesses a certain degree of predictive capability. The R^2 value exceeding 0.7 suggests that the model demonstrates good generalization ability and can be utilized for qualitative analyses. The R^2 value greater than 0.8 signifies that the model exhibits good predictive accuracy, and consequently, high credibility in remote sensing mapping and pollution tracing [32,5,33]. The smaller the MSE and MAE values, the higher the model accuracy.

4. Results and analysis

4.1. Patch size analysis

The input data scale directly impacts the network's performance. To improve the estimation accuracy, the optimal input window size was assessed by evaluating the input scale of the image blocks. Five input patch scales were considered: 5 × 5, 9 × 9, 13 × 13, 17 × 17, and 21 × 21. The estimation results using different input scales are listed in Table 4. At the 5 × 5 input scale, the network is able to capture the optimal features, and it exhibits a good predictive accuracy. On the test set, the 5 × 5 input scale presents the best estimation accuracy for the three water quality parameters, with the highest generalization capability. The R^2 accuracy values on the test set all exceed 0.8, specifically 0.8315, 0.8137, and 0.8245.

As the input patch size increases, the modeling accuracy decreases. The modeling results at the different scales suggest that the spatial heterogeneity of the hyperspectral imagery influences the feature expression of the deep network. Relatively large input scales contain

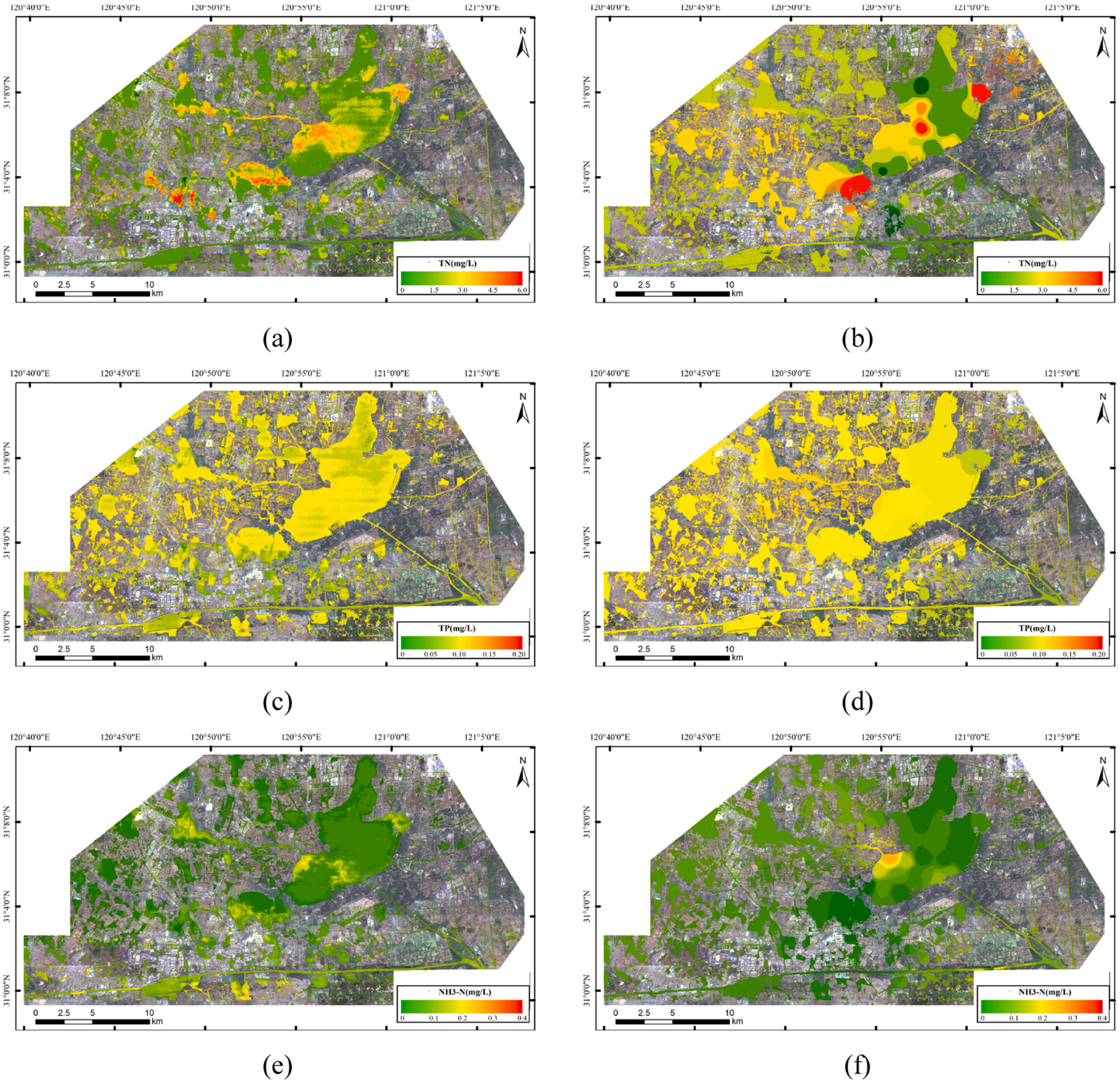

Fig. 5. Comparison between the concentration estimation distribution maps derived from hyperspectral imagery and spatial interpolation of the sampling point data.

Table 7
Statistics of the estimation results in the “One River and Three Lakes” region.

Region	Statistic	TN (mg/L)	TP (mg/L)	NH_3-N (mg/L)
Dianshan Lake	Min	1.34	0.061	0.036
	Max	3.57	0.117	0.278
	Mean	1.85	0.082	0.066
Yuandang Lake	Min	1.24	0.041	0.035
	Max	5.97	0.136	0.287
	Mean	2.97	0.077	0.083
Fen Lake	Min	1.33	0.044	0.060
	Max	1.67	0.104	0.291
	Mean	1.39	0.069	0.126
Taipu River	Min	1.31	0.021	0.015
	Max	1.84	0.127	0.207
	Mean	1.67	0.073	0.113

more spectral information, which affects the feature extraction, indicating that smaller spatial scales can extract more expressive nonlinear spatial features while preserving the spatial differences [19,34]. The final input scale of the model was set to 5 × 5, corresponding to a real spatial resolution of 3.75 m.

4.2. *Model accuracy comparison*

4.2.1. *Deep learning based regression model*

The results of the three deep regression models for water quality parameter estimation are listed in Table 5. Patch-DNNR without the SE module shows a decrease in training and test accuracy, compared to the Patch-CA-DNNR model. The R^2 values of TN, TP, and NH3-N for the test set show a decrease of 0.0722, 0.0776, and 0.1928, respectively. This suggests that the channel attention mechanism is crucial for extracting the interdependence between feature channels, which enhances the

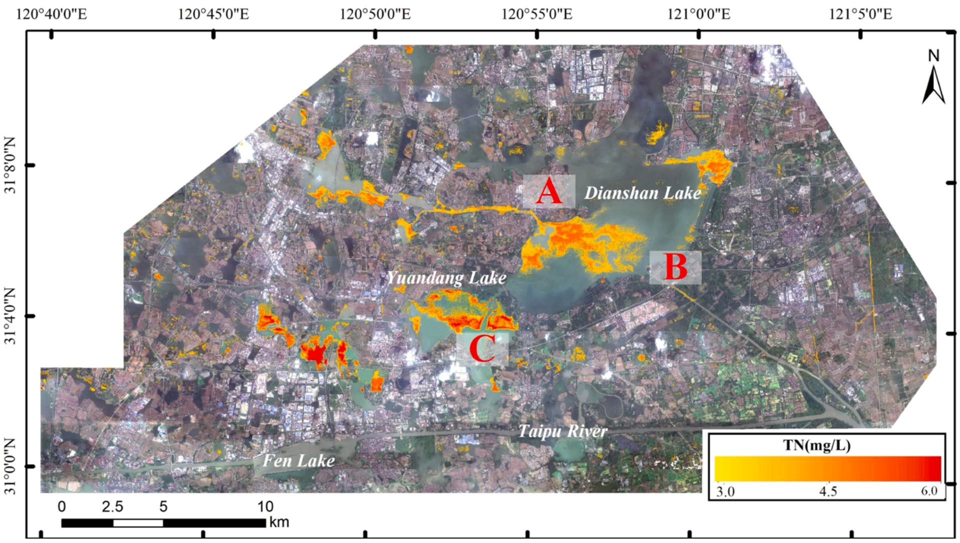

Fig. 6. Spatial distribution of the high TN concentration areas in the study area.

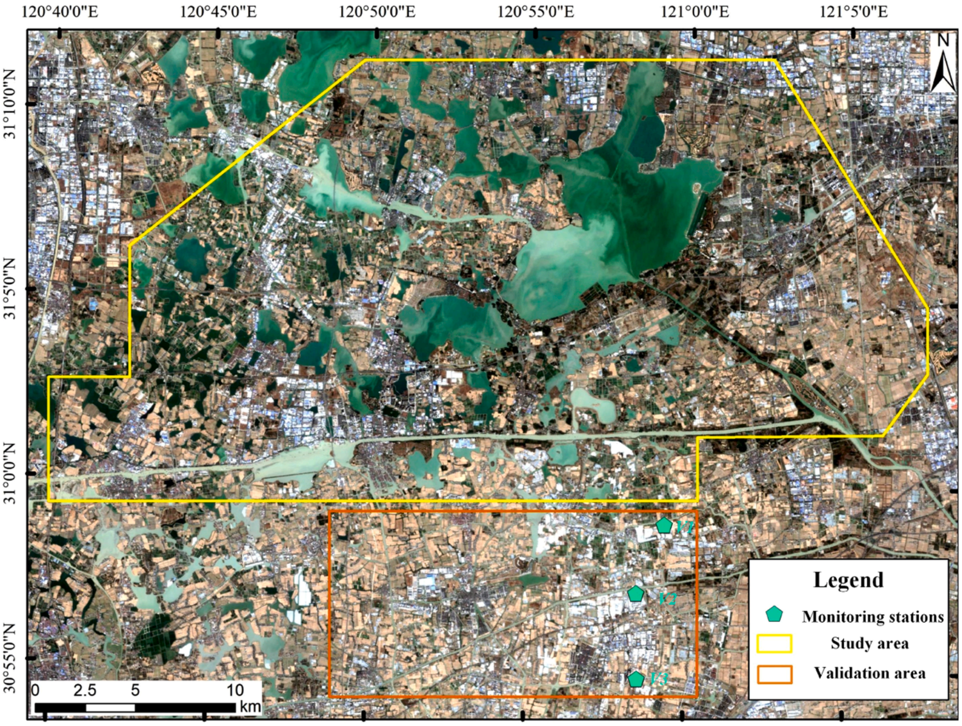

Fig. 7. The locations of the validation area and the monitoring stations in the validation area.

overall model performance for water quality parameter estimation.

Regarding the Pixel-DNNR model, which does not consider the spatial neighborhood information, the R^2 values of TN, TP, and NH3-N for the test set are 0.5381, 0.6384, and 0.7058, respectively, all of which are lower than the results of the patch-based model. It underscore the significant role that spatial features play in the accurate estimation of water quality parameters. The incorporation of image patches as input and the utilization of convolution operations represents an effective approach to capturing the spatial information within water bodies, resulting in a significant enhancement of model accuracy. The scatter plots of the estimated results are shown in Fig. 4.

4.2.2. *Feature analysis method*

Table 6 presents the estimation accuracy obtained using the different feature analysis methods in conjunction with the machine learning regression methods. The combinations of PCA-XGBoost, Pearson-XGBoost, and Pearson-RF achieve optimal prediction accuracies for the three water quality parameters, with the R^2 values for the training set reaching 0.9684, 0.9926, and 0.4348, respectively. However, the test set accuracies are comparatively low, with R^2 values of 0.5497, 0.4348, and 0.4488, respectively, indicating significant overfitting in the models. Overall, the traditional feature analysis methods demonstrate a limited capability in extracting features for the optically inactive water quality parameters. The R^2 values of the test sets are all below 0.6, and are significantly lower than those achieved by the deep learning based regression models. These results indicate that the traditional feature analysis methods are insufficient for the accurate estimation of water quality parameters.

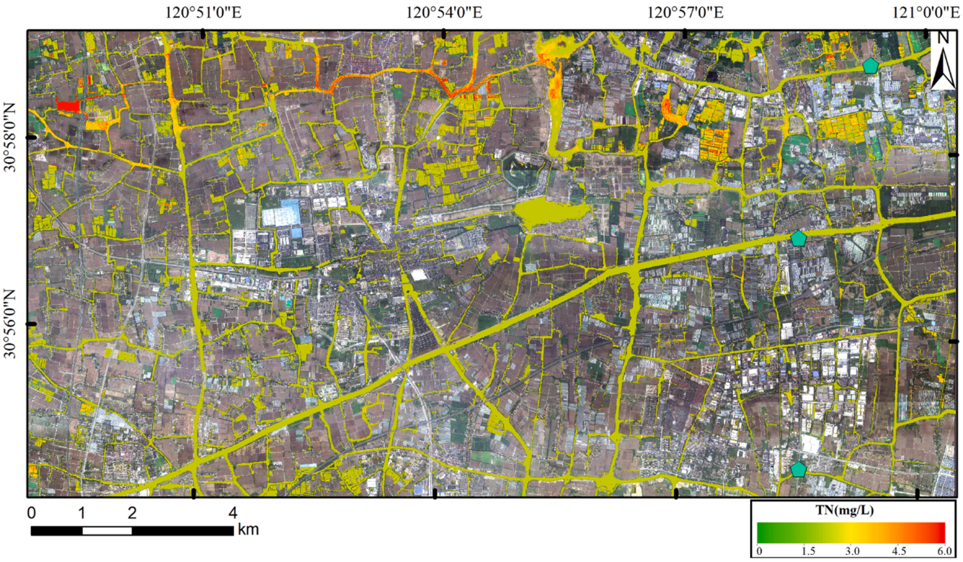

Fig. 8. Distribution maps of the estimated TN concentrations in the validation area.

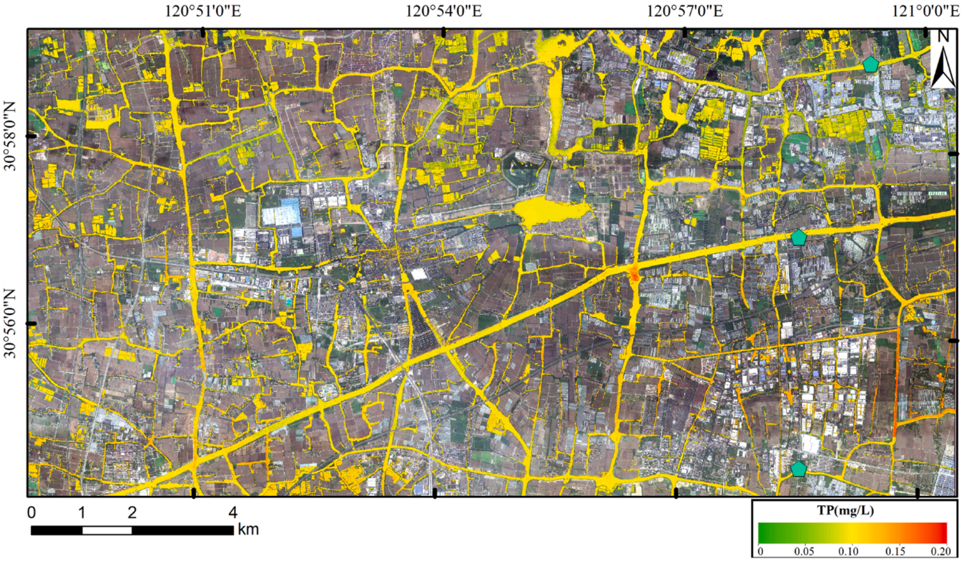

Fig. 9. Distribution maps of the estimated TP concentrations in the validation area.

4.3. Spatial distribution mapping of water quality parameter concentrations

The optimal deep regression model was selected for spatial distribution mapping of the water quality parameter concentrations. To validate the modeling effectiveness, the inverse distance weighting (IDW) interpolation method was applied to the sampled data within the study area. Fig. 5(a), (c), and (e) present the concentration distributions of the three water quality parameters—TN, TP, and NH3-N—estimated using hyperspectral imagery in the study area, and the spatial interpolation results based on the sampling point data are shown in Fig. 5(b), (d), and (f).

The spatial distribution reveals that the high-value regions of these water quality parameters are predominantly concentrated at the western inlet of Dianshan Lake. A clear diffusion trend can be observed as these nutrients flow into the lake, with the concentrations generally decreasing toward the southeastern outlet. For TN, distinct high-concentration zones can be identified in Dianshan Lake and parts of Yuandang Lake, with some northern areas of Lake Yuandang exceeding 4 mg/L. The spatial variation in TP and NH3-N concentrations across the study area is relatively minor. However, in the Taipu River and Fenhu Lake, NH3-N concentrations are significantly higher than those in the surrounding lake areas.

Comparing the spatial distribution maps estimated from airborne hyperspectral imagery with the spatial interpolation maps, it is apparent that the high-concentration areas identified by both methods are generally consistent. However, the hyperspectral imagery derived estimations provide significantly superior spatial details, compared to the interpolation results based on limited sampling data.

5. Discussion

5.1. Analysis of the nutrient pollution

Statistical analysis was conducted of the water quality parameters from the key areas of the “One River and Three Lakes” study area, with the results listed in Table 7. TN concentrations exhibit significant regional differences, with higher levels in Dianshan Lake (1.85 mg/L)

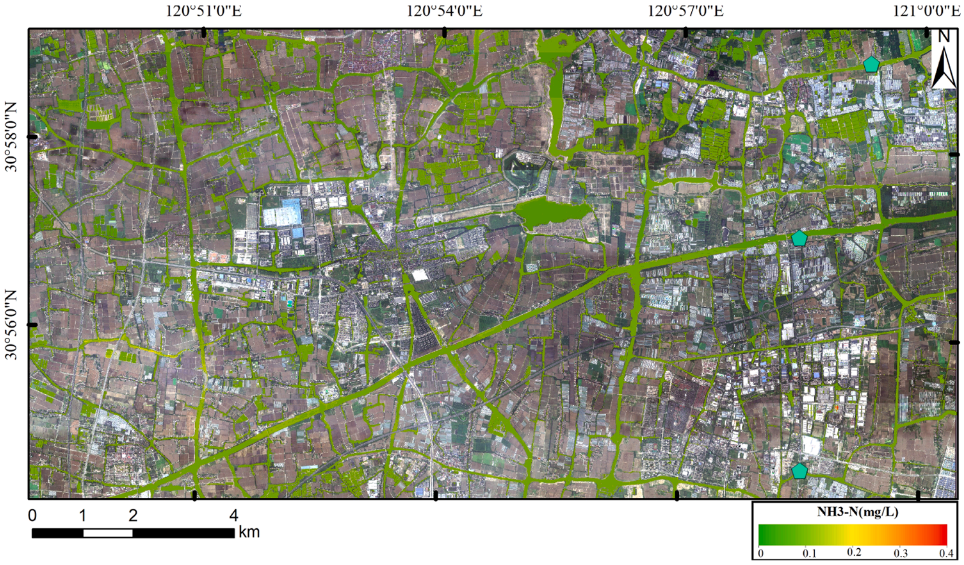

Fig. 10. Distribution maps of the estimated NH3-N concentrations in the validation area.

Table 8
Estimation accuracy of the water quality parameters in the validation area.

Parameter	Monitoring station	Measured (mg/L)	Estimated (mg/L)	Relative error (%)
TN	V1	2.495	2.632	5.491
	V2	2.875	2.737	4.800
	V3	3.192	2.650	16.967
TP	V1	0.112	0.090	19.804
	V2	0.114	0.097	14.864
	V3	0.145	0.112	22.759
NH3-N	V1	0.113	0.109	4.233
	V2	0.052	0.073	41.506
	V3	0.100	0.110	10.100

and Yuandang Lake (2.97 mg/L). TP concentrations are relatively stable across the region. NH_3-N concentrations are lower in Fenhu Lake and Taipu River, with average values of 0.126 mg/L and 0.113 mg/L, respectively.

To explore the spatial distribution of the polluted waters, regions with TN concentrations over 3 mg/L were identified, as shown in Fig. 6. The primary high value regions are found at the western inlet of Dianshan Lake (Region A) and Yuandang Lake (Region C). Region A, as the main inlet of Dianshan Lake, receives water primarily from the upstream Taihu Basin, which is of relatively poor quality. In addition, the surrounding lake area experiences significant human activity, with numerous industrial enterprises, poultry farming, agricultural pesticide usage, and residential zones contributing to large external loads of nitrogen and phosphorus through industrial wastewater discharge and agricultural non-point source pollution. This leads to a substantial burden of TN and TP in Dianshan Lake. The hydrological conditions of the study area play an important role in the observed spatial distribution of nutrient accumulation and eutrophication. According to a hydrological analysis of the study area [35], Jishui Port in Region A receives nearly 80 % of the total inflow. This substantial inflow is characterized by rapid water velocities at the inlet, resulting in a pronounced main channel. Furthermore, the accumulation of substantial organic matter in the bottom sediments of this area contributes to the nutrient enrichment [36,37]. The microbial decomposition of this organic matter releases significant levels of ammonium and phosphate [38], leading to internal pollution, which exacerbates the eutrophication of the water body. Region A also exhibits high phytoplankton biomass, with a dominance of cyanobacteria [39]. This dominance is indicative of a system with imbalanced nitrogen to phosphorus uptake ratios, potentially causing nutrient limitations for other phytoplankton species and an increased susceptibility to cyanobacterial blooms [40].

After entering Dianshan Lake from Region A, the spatial distribution of nutrients is influenced by the lake's hydrodynamic conditions. This results in a clear diffusion trend. Specifically, TN concentrations decrease at the eastern outlet in Region B. Several factors contribute to

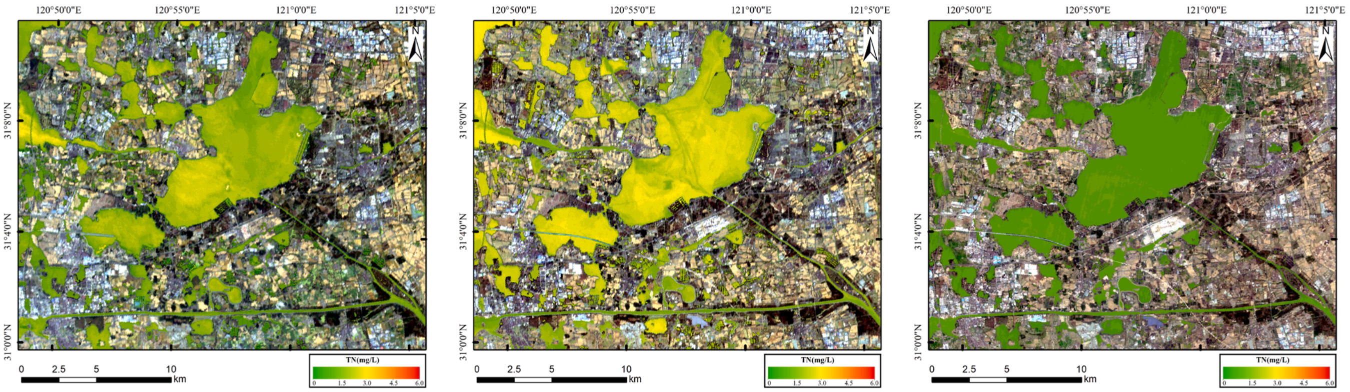

(a) 2021/11/18 (b) 2022/12/25 (c) 2023/3/6

Fig. 11. Distribution maps of the estimated TN concentrations obtained using satellite hyperspectral imagery.

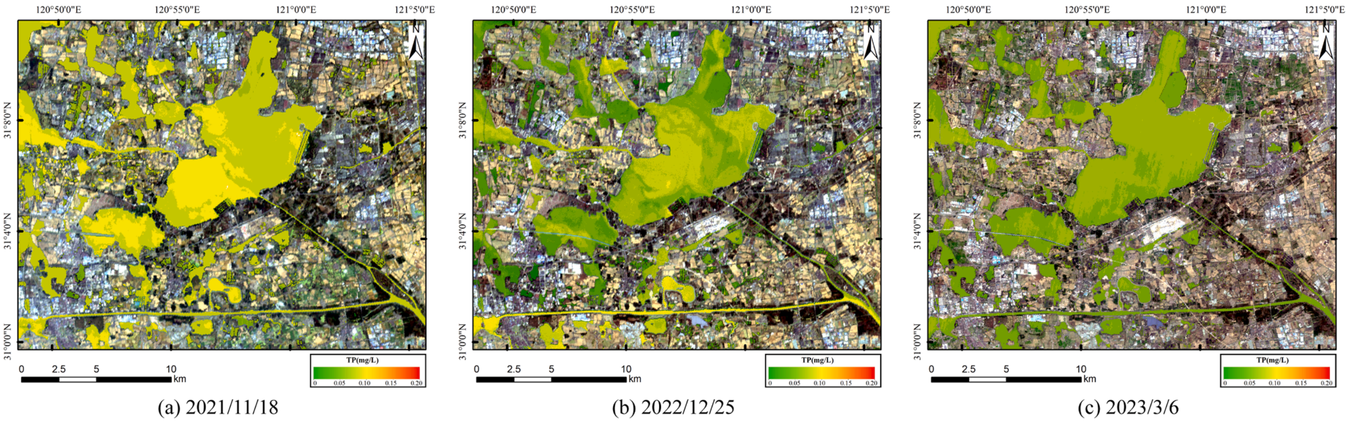

(a) 2021/11/18

(b) 2022/12/25

(c) 2023/3/6

Fig. 12. Distribution maps of the estimated TP concentrations obtained using satellite hyperspectral imagery.

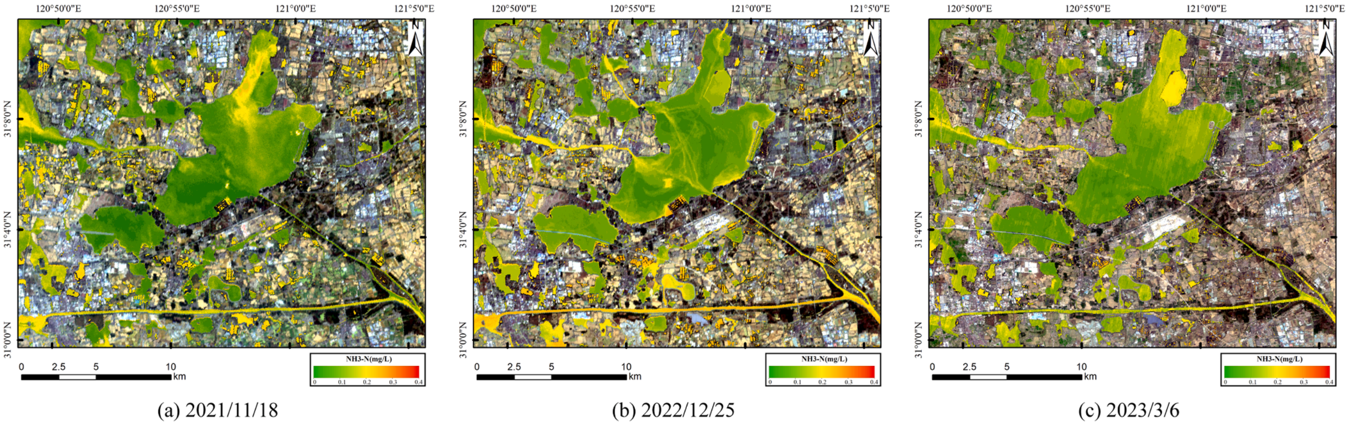

(a) 2021/11/18

(b) 2022/12/25

(c) 2023/3/6

Fig. 13. Distribution maps of the estimated NH3-N concentrations obtained using satellite hyperspectral imagery.

this reduction. First, the gradual deceleration of water flow facilitates the settling of suspended particulate matter, leading to the concomitant deposition of some nutrients into the bottom sediments. Second, aquatic plants within the lake assimilate a portion of the available nutrients. However, the relatively low coverage of aquatic vegetation in this region limits the overall nutrient uptake capacity [41,42]. Additionally, dilution effects also contribute to the reduction in nutrient concentrations. Based on field measurements [35], the Lanlu Port in Region B serves as the primary outflow channel of Dianshan Lake during the summer, accounting for 84 % of the total outflow. This indicates that the Lanlu Port near Region B is a major pathway for nutrient export from the lake.

Region C, where Yuandang Lake is located, has a relatively small water area, rendering it more vulnerable to external nutrient inputs and environmental disturbances, ultimately promoting eutrophication. The lake's aquatic vegetation is sparse, with low shoreline vegetation coverage and the presence of hard embankments. This negatively impacts the ecological hydrophilicity [43]. In addition, the lake's small outflow and long water residence time contribute to nutrient accumulation. This limited water volume restricts the lake's self-purification capacity, exacerbating the impact of the residential and agricultural non-point source pollution on its ecological environment. This pollution contributes to the elevated TN concentrations within the lake.

5.2. *Applicability analysis of deep regression models*

5.2.1. *Applicability analysis in areas without sample distribution*

To evaluate the model's applicability in areas lacking sample distribution, we utilized airborne hyperspectral imagery acquired on the afternoon of June 16, 2022, covering the validation area with three monitoring stations. The locations of the validation area and the monitoring stations are shown in Fig. 7. The well-trained Patch-CA-DNNR model was applied to the validation area to generate spatial distribution maps of three water quality parameters, as shown in Figs. 8–10.

Simultaneously with the acquisition of the airborne hyperspectral imagery, water quality data were collected from the monitoring stations for validation. The accuracy assessment results for the estimated water quality parameters are shown in Table 8. The average relative error calculations for the three water quality parameters are all below 20 %. The mean relative errors of TN, TP and NH3-N are 9.09 %, 19.14 % and 18.61 %, respectively. These results demonstrate the accuracy and generalizability of applying the model for water quality estimation in areas without sample distribution.

5.2.2. *Cross platform applicability analysis of deep regression models*

To further explore the generalizability of deep regression models across platforms and over extended time series, we transferred the trained deep learning based regression model to multi-temporal satellite hyperspectral imagery. Considering the relatively low spatial resolution (30 m) of satellite hyperspectral imagery, the input patch scale (5 × 5) of the proposed Patch-CA-DNNR unsuitable for small-scale river monitoring. Therefore, we utilized the well-trained Pixel-DNNR model trained on airborne hyperspectral imagery, as described in Section 4.1, for the satellite hyperspectral estimation and mapping. Three sets of satellite hyperspectral data acquired at different times were utilized for the validation. Detailed imaging information can be found in Section 2.2. To address the differences between spectral channels, band resampling was performed to align the spectral channels of the satellite

Table 9
Estimation accuracy of the water quality parameters using satellite hyperspectral imagery.

Parameter	Date	Monitoring station	Measured (mg/L)	Estimated (mg/L)	Relative error (%)
TN	2021/11/18	S1	1.280	1.561	21.988
		S2	2.173	1.759	19.017
		S3	1.350	1.609	19.135
		S4	2.068	1.711	17.287
	2022/12/25	S1	1.338	1.621	21.142
		S2	1.869	1.762	5.751
		S3	2.352	1.906	18.944
	2023/03/06	S1	2.190	1.209	44.785
		S2	1.684	1.448	14.033
		S3	2.432	1.198	50.721
TP	2021/11/18	S1	0.073	0.072	1.790
		S2	0.056	0.075	34.189
		S3	0.038	0.064	67.559
		S4	0.079	0.058	26.368
	2022/12/25	S1	0.152	0.087	43.053
		S2	0.097	0.077	20.445
		S3	0.076	0.075	0.159
	2023/03/06	S1	0.025	0.054	115.476
		S2	0.074	0.052	30.027
		S3	0.047	0.047	1.914
NH3-N	2021/11/18	S1	0.383	0.174	54.453
		S2	0.663	0.128	80.638
		S3	0.299	0.200	33.241
		S4	0.089	0.103	16.904
	2022/12/25	S1	–	–	–
		S2	0.311	0.205	33.962
		S3	0.165	0.169	2.133
	2023/03/06	S1	0.165	0.150	9.029
		S2	0.297	0.182	38.699
		S3	0.119	0.150	25.461

Table 10
Estimation accuracy of TP and NH3-N using satellite hyperspectral imagery after model fine-tuning.

Parameter	Date	Monitoring station	Measured (mg/L)	Estimated (mg/L)	Relative error (%)
TP	2021/11/18	S1	0.073	0.068	6.849
		S2	0.056	0.073	30.357
		S3	0.038	0.058	52.632
		S4	0.079	0.054	31.646
	2022/12/25	S1	0.152	0.087	42.763
		S2	0.097	0.080	17.526
		S3	0.076	0.072	5.263
	2023/03/06	S1	0.025	0.034	36.721
		S2	0.074	0.054	27.027
		S3	0.047	0.042	10.638
NH3-N	2021/11/18	S1	0.383	0.279	27.154
		S2	0.663	0.518	33.937
		S3	0.299	0.212	29.097
		S4	0.089	0.123	38.202
	2022/12/25	S1	–	–	–
		S2	0.311	0.245	21.221
		S3	0.165	0.189	14.545
	2023/03/06	S1	0.165	0.153	7.273
		S2	0.297	0.216	27.273
		S3	0.119	0.157	31.932

imagery with the model input channels. The resulting spatial distributions of water quality parameter concentrations derived from the satellite hyperspectral imagery are presented in Figs. 11–13.

For validation, we selected water quality monitoring station data that were temporally closest to image acquisition. The station's location is shown in Fig. 1. Some monitoring data were unavailable due to station maintenance. A comparison between the estimated results and the monitoring station data is shown in Table 9. The average relative error calculations reveal that the errors for the three water quality parameters are all below 35 %, with TN achieving the highest accuracy, with an average relative error of approximately 23.28 %. The average relative errors of TP and NH3-N are 34.10 % and 32.72 %, respectively. These validation results demonstrate that the deep learning model exhibits a level of transferability and can achieve a relatively good prediction accuracy in cross-platform, long-term time-series data.

Unlike models based on spectral mechanisms, the data-driven deep regression models can exhibit limitations in cross-platform and multi-temporal data transferability. This is primarily due to the restricted sample inputs and specific training patterns inherent in these models. To further investigate this issue, we analyzed the concentration distribution ranges of the samples for each water quality parameter utilized in the model training, as well as the distribution of the monitoring station data across the various time periods. The analysis reveals that the TN concentration range of 1.28–2.43 mg/L matches the modeling data range, resulting in a high prediction accuracy. In contrast, the TP and NH3-N monitoring data show significant discrepancies with the modeling data, leading to inaccurate estimates outside the training range. For example, on March 6, 2023, the TP concentration at station S1 was 0.025 mg/L, which is much lower than the minimum modeling value of 0.043 mg/L, resulting in a relative error of 115 %. Similarly, on November 18, 2021, at station S2, the NH3-N concentration was 0.663 mg/L, exceeding the maximum modeling value of 0.28 mg/L, with a relative error of 80 %. After removing validation points with large discrepancies, the average relative errors for TP and NH3-N decrease to 25.06 % and 26.74 %, respectively.

The inherent dynamism of aquatic ecosystems manifests as continuous fluctuations in water quality parameters. Consequently, a significant time span between the validation and modeling datasets can lead to discrepancies in the data range, causing a suboptimal estimation performance for certain samples. Data-driven deep regression models are inherently dependent on the distribution of the existing datasets to learn patterns and relationships. This reliance can limit the models' effectiveness when applied to cross-platform and long-term scenarios, especially when the models are trained on single-period data. Therefore, the constraints related to sample size and observation methods highlight the potential limitations in the transferability and robustness of such models across different platforms and extended timeframes.

To address this limitation, we employed a fine-tuning strategy, retraining the model with synthetic data generated from the original hyperspectral dataset. Specifically, we created new training samples by pairing the original hyperspectral data with predicted values representing an extremely low TP concentration and an extremely high NH3-N concentration. We then fine-tuned the TP and NH3-N models using this expanded dataset. The estimation results after fine-tuning are presented in Table 10. The prediction accuracy for extreme values of TP and NH3-N was significantly improved, with the relative error decreasing from 115.476 % and 80.638–36.721 % and 33.937 %, respectively. These results demonstrate improved model performance in predicting out-of-range values, thereby enhancing the model's generalizability. For future applications, data from automated water quality monitoring stations can be used as input samples to continuously fine-tune the model, further enhancing its generalizability.

5.3. *Interpretability analysis of deep regression model*

Deep regression models demonstrate a strong nonlinear fitting abilities in water quality parameter regression. To better understand the complex relationships between spectral features and these parameters, we conducted an interpretability analysis of the proposed deep regression model. The three water quality parameters analyzed in this study are optically inactive and cannot be directly retrieved from spectral absorption. Therefore, we first analyzed the correlations between the first-derivative water spectra and the three water quality parameters. Fig. 14 shows that the parameters correlate most strongly with spectra

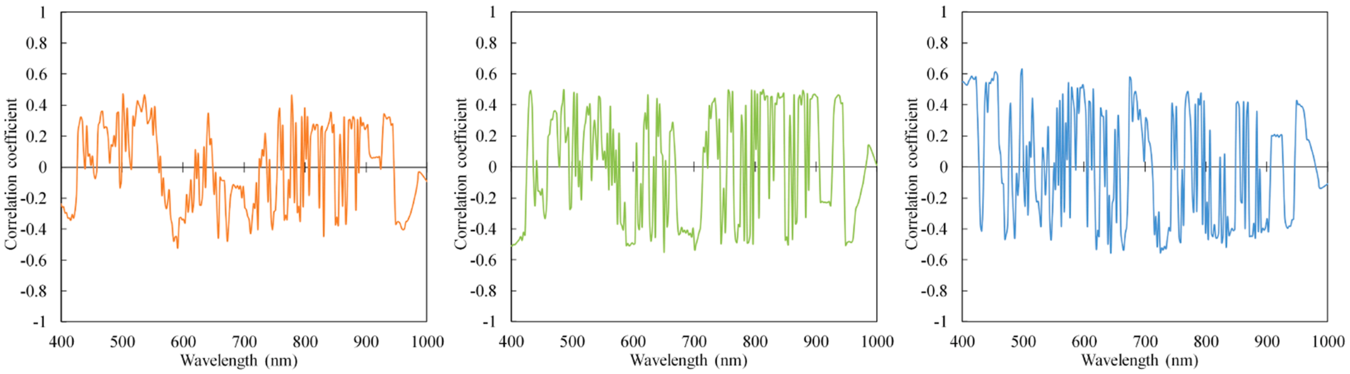

(a) TN (b) TP (c) NH3-N

Fig. 14. Distribution of correlation coefficient between first-derivative water spectra and the three water quality parameters.

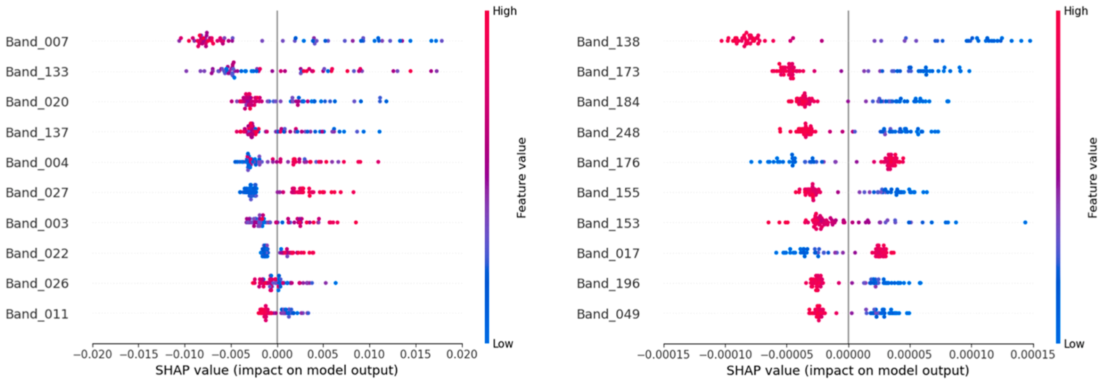

(a) TN (b) TP

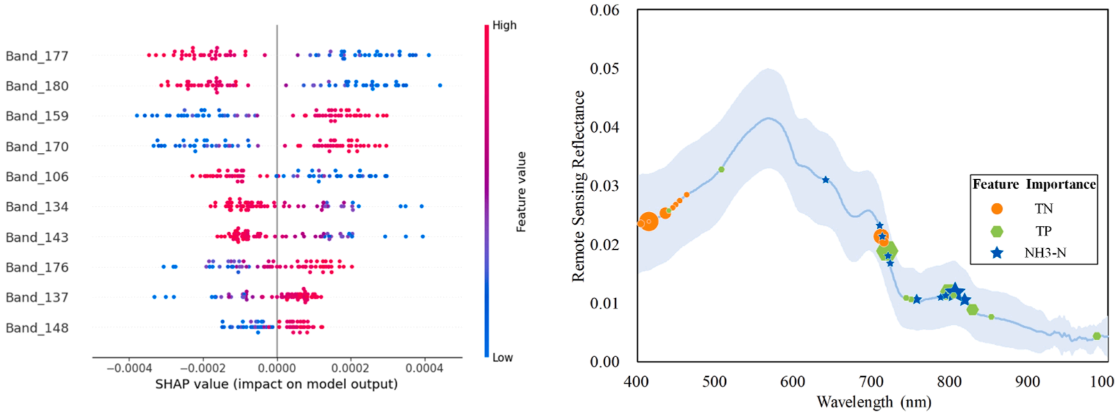

(c) NH3-N (d) Distribution of bands

Fig. 15. Visualization of spectral band importance and distribution of the proposed deep regression model using SHAP method. (a) to (c) display scatter plots of spectral importance for TN, TP, and NH3-N, respectively. The vertical axis in each plot represents the ten bands with the highest feature weights, ordered from top to bottom. The horizontal axis indicates the spectral importance value for each sample. (d) illustrates the distribution of these bands, where symbol size corresponds to feature importance. The curve represents the mean reflectance of the water samples, and the shaded area represents the mean ± standard deviation.

around 430 nm (blue region) and 600–680 nm (red region). These spectral bands align with the characteristic absorption and reflectance regions of Chl-a, suggesting that nutrient parameters in the study area are influenced by algal activity and are associated with Chl-a spectral signature [44,45]. Furthermore, a high correlation was observed in the 800 nm near-infrared region, which is consistent with the characteristic spectral band of suspended particulate matter reflectance [46]. This finding indicates that these parameters are related to water color parameters. Consequently, deep regression models can effectively utilize spectral features associated with both Chl-a and suspended particulate matter, as well as inherent spectral correlations within the water body, to quantitatively estimate these parameters.

Subsequently, we utilized SHapley Additive exPlanations (SHAP) model [47] to quantify the contribution of each input spectral band to the model predictions and to reveal feature impacts at the sample level. For each sample, we calculated feature weights for each input channel and selected the top 10 bands with the highest absolute weights. The scatter plots illustrating the impact on model output are shown in Fig. 15 (a) to (c).

Analysis of SHAP values revealed that for TN, the most influential spectral bands were clustered around 430 nm, corresponding to the absorption peak of chlorophyll-a. This finding suggests that the proposed deep regression model relied on Chl-a related spectral characteristics when predicting TN. TP and NH3-N exhibited distinct feature distributions. The most influential spectral bands were clustered around 700 nm and 800 nm. This indicates that the deep learning model, when predicting TP and NH3-N, leveraged spectral information associated with both Chl-a and suspended particulate matter.

Leveraging the model interpretability provided by SHAP, we can not only uncover the intrinsic mechanisms of deep learning models in predicting optically inactive water quality parameters, but also discover potentially relevant spectral features associated with water color parameters. This enhances our understanding of how models leverage spectral information for prediction and provides more refined guidance for remote sensing estimation.

5.4. Limitations and future research

Compared to traditional environmental monitoring methods, deep learning models offer significant advantages in handling complex nonlinear data, extracting hidden spectral response, and predicting future trends. The resulting improvement in prediction accuracy is crucial for accurate mapping and timely warning of nutrient pollution. However, deep learning methods still possess inherent limitations. Firstly, deep learning models typically require substantial amounts of training data, while the acquisition of remote sensing data and synchronous water quality monitoring data is often constrained by temporal and spatial limitations. Secondly, the internal mechanisms of deep learning models are typically intricate. While methods like SHAP can be used to analyze spectral correlation characteristics, the specific meaning of network parameters is difficult to discern, resulting in a relatively low level of interpretability. This can be a challenge in certain environmental studies that require understanding specific contributing factors. Furthermore, the generalization ability of deep learning models may be limited when faced with new and unknown environmental conditions. Therefore, while deep learning methods hold significant potential in environmental monitoring, their model training still relies on traditional environmental monitoring methods such as laboratory analysis and real-time monitoring at monitoring stations. These traditional methods not only provide the precise ground truth data required for model training and validation, but also enable in-depth analysis of specific pollutants and long-term monitoring of complex environmental changes, thereby providing indispensable support for environmental management and decision-making.

To fully realize the potential of deep learning in the realm of environmental monitoring, future research should focus on addressing the limitations related to data availability and model interpretability. A key research direction will be exploring how to integrate the strengths of traditional methods and deep learning techniques to develop more efficient and reliable environmental monitoring technologies. This includes combining hydrological and water quality mechanistic models with deep learning frameworks to construct more transparent and interpretable deep neural networks. Furthermore, to improve model robustness and generalization ability, we should fully utilize multi-source datasets across diverse water systems and conditions to iteratively train the models, enhancing their robustness and generalizability. Finally, to facilitate the practical application of these advancements, future work should investigate the establishment of cloud platforms that integrate multi-source remote sensing and water quality data, enabling real-time water environment monitoring. These platforms would provide environmental professionals with key features such as pollutant concentration prediction, risk assessment, and decision support, offering robust support for future monitoring programs and informed environmental management strategies.

6. Conclusion

This study addressed the challenge of the estimation of water quality parameters using hyperspectral imagery. An innovative multi-parameter regression network, utilizing image blocks and a channel attention mechanism, was constructed to achieve accurate estimation and distribution mapping of the eutrophication-related water quality parameters. The proposed patch-based channel attention deep regression network achieved strong performance ($R^2 > 0.8$) and a 30 % accuracy improvement over traditional methods.

Nutrient maps derived from multi-temporal and multi-source hyperspectral imagery effectively visualized pollution distribution. The robustness of the model was further demonstrated through applicability analysis and interpretability analysis. The findings of this study provide a powerful tool for the dynamic monitoring of nutrient pollution in water bodies. However, the deep learning approach’s reliance on training data distribution restricts its effectiveness in cross-platform and long-term applications, particularly for single-period models. Future efforts should focus on combining mechanistic models with interpretable deep neural networks, utilizing multi-source data for robust training. These efforts will contribute to the development of more robust and adaptable environmental monitoring technologies for water resource management.

Environmental implication

This research presents a novel approach on the precise mapping of eutrophication pollution in inland water bodies by leveraging multi-source hyperspectral data and advanced deep regression network. Through an innovative deep convolutional spatial-spectral joint learning framework, it effectively extracts critical features from hyperspectral data, significantly enhancing the accuracy of eutrophication-related water quality parameter estimations. The robustness demonstrated by this method across multi-platforms and multi-temporal imagery highlights its potential for water environment monitoring. This research not only advances the precision of water quality monitoring but also provides method for understanding and long-term management of eutrophication-driven water pollution.

CRediT authorship contribution statement

Niu Chao: Writing – original draft, Visualization, Validation, Software, Methodology, Formal analysis. **Tan Kun:** Writing – review & editing, Supervision, Methodology, Funding acquisition. **Wang Xue:** Writing – review & editing, Investigation, Data curation. **Pan Chen:** Resources, Data curation.

Declaration of Competing Interest

The authors declare that they have no known competing financial interests or personal relationships that could have appeared to influence the work reported in this paper.

Acknowledgements

This work was supported by the National Natural Science Foundation of China [Grant No. 42171335]; the Shanghai Municipal Science and Technology Major Project [Grant No. 22511102800]; the National Civil Aerospace Project of China [Grant No. D040102]; the China Postdoctoral Science Foundation [Grant No. 2024M760925]; the Yangtze River Delta Science and Technology Innovation Community Joint Research (Basic Research) Project [Grant No. 2024CSJZN1300].

Data availability

The data that has been used is confidential.

References

[1] Erler, A.R., Frey, S.K., Khader, O., d'Orgeville, M., Park, Y.J., Hwang, H.T., et al., 2019. Simulating climate change impacts on surface water resources within a lake-affected region using regional climate projections. Water Resour Res 55 (1), 130–155.

[2] Chislock, M.F., Doster, E., Zitomer, R.A., Wilson, A.E., 2013. Eutrophication: causes, consequences, and controls in aquatic ecosystems. Nat Educ Knowl 4 (4), 10.

[3] Zamparas, M.G., Kyriakopoulos, G.L., 2021. Chemical lake restoration. Springer.

[4] Giri, S., 2021. Water quality prospective in twenty first century: status of water quality in major river basins, contemporary strategies and impediments: a review. Environ Pollut 271, 116332.

[5] Gholizadeh, M., Melesse, A., Reddi, L., 2016. A comprehensive review on water quality parameters estimation using remote sensing techniques. Sensors 16 (8), 1298.

[6] Dekker, A.G., Vos, R., Peters, S., 2002. Analytical algorithms for lake water TSM estimation for retrospective analyses of TM and SPOT sensor data. Int J Remote Sens 23 (1), 15–35.

[7] Kutser, T., Arst, H., Miller, T., Käärmann, L., Milius, A., 1995. Telespectrometrical estimation of water transparency, chlorophyll-a and total phosphorus concentration of Lake Peipsi. Int J Remote Sens 16 (16), 3069–3085.

[8] Zhang, H., Huo, S., Feng, L., Ma, C., Li, W., Liu, Y., et al., 2024. Geographic characteristics and meteorological factors dominate the variation of chlorophyll-a in lakes and reservoirs with higher TP concentrations. Water Resour Res 60 (6) e2023WR036587.

[9] Lin, Y., Li, L., Yu, J., Hu, Y., Zhang, T., Ye, Z., et al., 2021. An optimized machine learning approach to water pollution variation monitoring with time-series Landsat images. Int J Appl Earth Obs Geoinf 102, 102370.

[10] Oiry, S., Barillé, L., 2021. Using sentinel-2 satellite imagery to develop microphytobenthos-based water quality indices in estuaries. Ecol Indic 121, 107184.

[11] Olmanson, L.G., Brezonik, P.L., Bauer, M.E., 2013. Airborne hyperspectral remote sensing to assess spatial distribution of water quality characteristics in large rivers: The Mississippi River and its tributaries in Minnesota. Remote Sens Environ 130, 254–265.

[12] Jović, A., Brkić, K. and Bogunović, N. 2015 A review of feature selection methods with applications, pp. 1200-1205, Ieee.

[13] Chen, Y., Jiang, H., Li, C., Jia, X., Ghamisi, P., 2016. Deep feature extraction and classification of hyperspectral images based on convolutional neural networks. IEEE Trans Geosci Remote Sens 54 (10), 6232–6251.

[14] Cao, Y., Ye, Y., Zhao, H., Jiang, Y., Wang, H., Shang, Y., et al., 2018. Remote sensing of water quality based on HJ-1A HSI imagery with modified discrete binary particle swarm optimization-partial least squares (MDBPSO-PLS) in inland waters: a case in Weishan Lake. Ecol Inform 44, 21–32.

[15] Yang, H., Kong, J., Hu, H., Du, Y., Gao, M., Chen, F., 2022. A review of remote sensing for water quality retrieval: progress and challenges. Remote Sens 14 (8), 1770.

[16] Valadkhan, D., Moghaddasi, R., Mohammadinejad, A., 2022. Groundwater quality prediction based on LSTM RNN: an Iranian experience. Int J Environ Sci Technol 19 (11), 11397–11408.

[17] Parmar, N., Vaswani, A., Uszkoreit, J., Kaiser, L., Shazeer, N., Ku, A., et al., 2018. Image transformer. PMLR, pp. 4055–4064.

[18] Koponen, S., Pulliainen, J., Kallio, K., Hallikainen, M., 2002. Lake water quality classification with airborne hyperspectral spectrometer and simulated MERIS data. Remote Sens Environ 79 (1), 51–59.

[19] Niu, C., Tan, K., Jia, X., Wang, X., 2021. Deep learning based regression for optically inactive inland water quality parameter estimation using airborne hyperspectral imagery. Environ Pollut 286, 117534.

[20] Pyo, J., Ligaray, M., Kwon, Y., Ahn, M.-H., Kim, K., Lee, H., et al., 2018. High-spatial resolution monitoring of phycocyanin and chlorophyll-a using airborne hyperspectral imagery. Remote Sens 10 (8), 1180.

[21] Zhang, J., Zhang, L., Chai, Q., Shen, Y., Ji, L., Zhao, Q., et al., 2021. Insights into spatiotemporal variations of the water quality in Taihu Lake Basin, China. Environ Monit Assess 193, 1–20.

[22] Xiong, G., Wang, G., Wang, D., Yang, W., Chen, Y., Chen, Z., 2017. Spatio-temporal distribution of total nitrogen and phosphorus in Dianshan lake, China: the external loading and self-purification capability. Sustainability 9 (4), 500.

[23] Niu, C., Tan, K., Wang, X., Han, B., Ge, S., Du, P., et al., 2021. Radiometric cross-calibration of the ZY1-02D hyperspectral imager using the GF-5 AHSI imager. IEEE Trans Geosci Remote Sens 60, 1–12.

[24] Niu, C., Tan, K., Wang, X., Du, P., Pan, C., 2024. A semi-analytical approach for estimating inland water inherent optical properties and chlorophyll a using airborne hyperspectral imagery. Int J Appl Earth Obs Geoinf 128, 103774.

[25] Hu, J., Shen, L. and Sun, G. 2018 Squeeze-and-excitation networks, pp. 7132-7141.

[26] Galindo-Prieto, B., Eriksson, L., Trygg, J., 2014. Variable influence on projection (VIP) for orthogonal projections to latent structures (OPLS). J Chemom 28 (8), 623–632.

[27] Tan, K., Ma, W., Chen, L., Wang, H., Du, Q., Du, P., et al., 2021. Estimating the distribution trend of soil heavy metals in mining area from HyMap airborne hyperspectral imagery based on ensemble learning. J Hazard Mater 401, 123288.

[28] Höskuldsson, A., 1988. PLS regression methods. J Chemom 2 (3), 211–228.

[29] Brereton, R.G., Lloyd, G.R., 2010. Support vector machines for classification and regression. Analyst 135 (2), 230–267.

[30] Belgiu, M., Drăguţ, L., 2016. Random forest in remote sensing: a review of applications and future directions. ISPRS J Photogramm Remote Sens 114, 24–31.

[31] Chen, T. and Guestrin, C. 2016 Xgboost: A scalable tree boosting system, pp. 785-794.

[32] Carpenter, D., Carpenter, S., 1983. Modeling inland water quality using Landsat data. Remote Sens Environ 13 (4), 345–352.

[33] Topp, S.N., Pavelsky, T.M., Jensen, D., Simard, M., Ross, M.R., 2020. Research trends in the use of remote sensing for inland water quality science: moving towards multidisciplinary applications. Water 12 (1), 169.

[34] Pyo, J., Duan, H., Baek, S., Kim, M.S., Jeon, T., Kwon, Y.S., et al., 2019. A convolutional neural network regression for quantifying cyanobacteria using hyperspectral imagery. Remote Sens Environ 233, 111350.

[35] Li, W., Yang, C., Pan, Z., 2013. Analysis on the festival hydrological characteristics of the Dianshan Lake. Trans Oceanol Limnol 1, 131–136.

[36] Jiang, X., Gao, G., Zhang, L., Tang, X., Shao, K., Hu, Y., 2020. Denitrification and dissimilatory nitrate reduction to ammonium in freshwater lakes of the Eastern Plain, China: influences of organic carbon and algal bloom. Sci Total Environ 710, 136303.

[37] Li, Y., Tu, Y., Sun, T., Duan, Y., Kou, J., Li, W., et al., 2024. Source apportionment of organic carbon and nitrogen in sediments from river and lake in the highly urbanized Changjiang Delta. J Hazard Mater 478, 135590.

[38] Chen, J., Jin, Q., Shi, R., Xu, X., Zhao, S., Ji, M., et al., 2020. Synchronous nutrient controlled-release of greenhouse gases during mineralization of sediments from different lakes. Bull Environ Contam Toxicol 105, 76–85.

[39] Yang, L., Zhang, W., Shang, G., Zhang, J., Wang, L., Wei, H., 2018. Succession characteristics of phytoplankton functional groups and their relationships with environmental factors in Dianshan Lake, Shanghai. Environ Sci 39 (7), 3158–3167.

[40] Liu, X., Chen, L., Zhang, G., Zhang, J., Wu, Y., Ju, H., 2021. Spatiotemporal dynamics of succession and growth limitation of phytoplankton for nutrients and light in a large shallow lake. Water Res 194, 116910.

[41] Bornette, G., Puijalon, S., 2011. Response of aquatic plants to abiotic factors: a review. Aquat Sci 73, 1–14.

[42] Deng, H.-g, Zhang, J., Wu, J.-j, Yao, X., Yang, L.-w, 2020. Biological denitrification in a macrophytic lake: implications for macrophytes-dominated lake management in the north of China. Environ Sci Pollut Res 27, 42460–42471.

[43] Yongqing, M., Wangrui, L., Jiawei, W., Andi, L., Jielong, Z., 2022. Water ecological restoration practice of cross-administrative-area synergic projects–case study on the Yuandang lake synergic eco-development pilot project, the demonstration zone of green and integrated ecological development of Yangtze River Delta. Landsc Archit Front 10 (6).

[44] Neil, C., Spyrakos, E., Hunter, P.D., Tyler, A.N., 2019. A global approach for chlorophyll-a retrieval across optically complex inland waters based on optical water types. Remote Sens Environ 229, 159–178.

[45] Sakuno, Y., Hatakeyama, K., Miyamoto, Y., Hatsuda, A., Mori, A., Kuki, T., 2014. Relationship between spectral reflectance and chlorophyll-a concentration in the eutrophic Lake Togo-ike. SPIE, pp. 102–108.

[46] Doxaran, D., Froidefond, J.-M., Lavender, S., Castaing, P., 2002. Spectral signature of highly turbid waters: application with SPOT data to quantify suspended particulate matter concentrations. Remote Sens Environ 81 (1), 149–161.

[47] Lundberg, S. 2017. A unified approach to interpreting model predictions. arXiv preprint arXiv:1705.07874.